SCIENTIFIC REP⚙RTS

OPEN

Approach to multifunctional device platform with epitaxial graphene on transition metal oxide

Jeongho Park[1], Tyson Back[1,2,3], William C. Mitchel[1], Steve S. Kim[1], Said Elhamri[4], John Boeckl[1], Steven B. Fairchild[1], Rajesh Naik[1] & Andrey A. Voevodin[1]

Heterostructures consisting of two-dimensional materials have shown new physical phenomena, novel electronic and optical properties, and new device concepts not observed in bulk material systems or purely three dimensional heterostructures. These new effects originated mostly from the van der Waals interaction between the different layers. Here we report that a new optical and electronic device platform can be provided by heterostructures of 2D graphene with a metal oxide (TiO_2). Our novel direct synthesis of graphene/TiO_2 heterostructure is achieved by C_{60} deposition on transition Ti metal surface using a molecular beam epitaxy approach and O_2 intercalation method, which is compatible with wafer scale growth of heterostructures. As-grown heterostructures exhibit inherent photosensitivity in the visible light spectrum with high photo responsivity. The photo sensitivity is 25 times higher than that of reported graphene photo detectors. The improved responsivity is attributed to optical transitions between O 2p orbitals in the valence band of TiO_2 and C 2p orbitals in the conduction band of graphene enabled by Coulomb interactions at the interface. In addition, this heterostructure provides a platform for realization of bottom gated graphene field effect devices with graphene and TiO_2 playing the roles of channel and gate dielectric layers, respectively.

Graphene (Gr) is a very attractive material for diverse optoelectronic and electronic device applications due to its extraordinary transport properties, broad spectral-bandwidth, and fast response time[1–4]. For many applications, dielectrics layers such as SiO_2 play a crucial role in device operation. In graphene field effect transistors (GFET), graphene provides the active layer where the channel carriers are modulated by gate biasing through the dielectric layer. In graphene optical devices a dielectric layer is needed to induce a built-in potential within the structure so that photo-excited electrons can be extracted from the photosensitive materials into the graphene layer on top. Currently the photosensitive 2D materials such as MoS_2 or WS_2 are widely investigated to enhance photo-responsibility. Recent studies of graphene/ photosensitive 2D heterostructures have revealed new physical phenomena such as Moire patterns[5,6], new Dirac points[7], and the Hofstadter butterfly[8,9]. These originate from the van der Waals interaction at the interface. The observation of significant improvement of quantum efficiency in Gr/WS_2/Gr hetero-structure resulted from Van Hove singularities[10] originated from van der Waals interaction. Due to the lack of direct growth methods, however, fabrication is typically done by exfoliation or transfer methods. Here, we propose new direct growth approach to structure graphene/a photosensitive material and report its dual function (bottom gated FET and photodetector) that make it a unique hybrid device. In this studies, TiO_2 has been considered since it is a well-known material that has been widely used for light harvesting[11] as well as a high dielectric constant (~100). These dual characteristics make TiO_2 a very

[1]Air Force Research Laboratory, Materials and Manufacturing Directorate (AFRL/RXA) Wright-Patterson AFB, OH 45433-7707. [2]University of Dayton Research Institute, Dayton, Ohio 45469-0170, USA. [3]Center of Excellence for Thin Film Research and Surface Engineering, University of Dayton, Dayton, Ohio 45469-0170, USA. [4]Departments of Physics, University of Dayton, Dayton, Ohio 45469. Correspondence and requests for materials should be addressed to J.P. (email: jeongho.park@wpafb.af.mil)
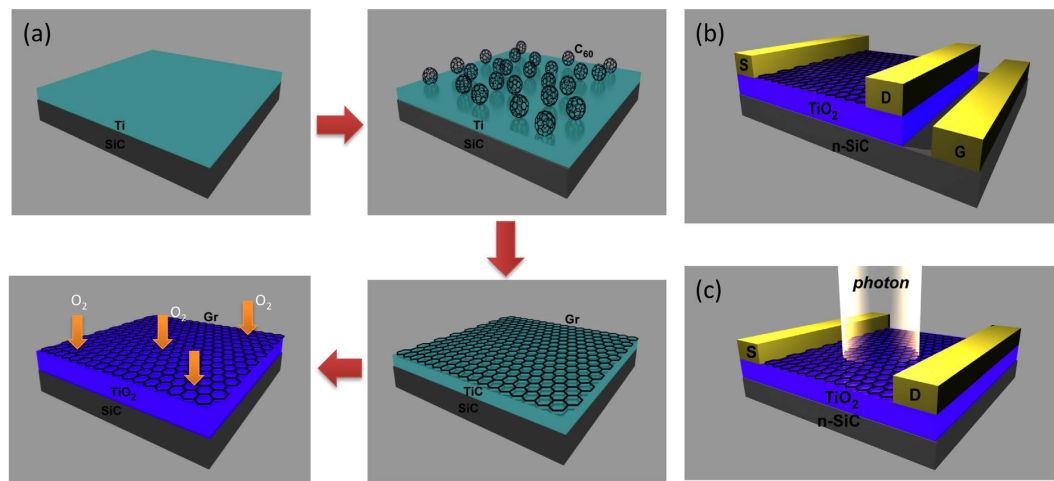
Figure 1. The schematic diagram of Gr/TiO₂ structure growth and the configuration of its electronic and optical device. (**a**) The C_{60} is deposited on Ti/SiC to grow graphene. After C_{60} deposition, Ti metal converts into TiC by carbon reduction. By O_2 intercalation of graphene/TiC/SiC structure, the finial graphene/TiO₂/SiC heterostructure is obtained. (**b**) Configuration of bottom gated FET device. (**c**) Configuration of photo response measurement.

attractive material for the realization of both electronic and photonic devices. The schematic diagram of our growth approach is shown in Fig. 1a. The as-grown heterostructure displays both photosensitivity under visible light and field effect phenomena when the gate voltage through the underneath TiO₂ dielectric layer. We demonstrate this dual functionality by depositing two top metal contacts on the Gr/TiO₂ heterostructure to serve as source and drain electrodes. The gating voltage is applied through the underlying TiO₂ on n-type SiC in a bottom gated FET configuration. With the same device configuration, the photosensitivity under visible light illumination is measured by the change of photoconductivity with zero gate voltage. We believe that the observed photo response at zero gate voltage is caused by the optical transitions between the valence band maximum, associated O 2p orbitals in TiO₂, and the conduction band minima, formed by the C 2p orbitals of the graphene in the Gr/TiO₂ heterostructure. The schematic diagrams of device and measurement configurations are shown in Fig. 1b,c. The electrical transport experiments to characterize Gr/TiO₂ heterostructure have been conducted in air.

Results

The growth of graphene. To investigate the graphene growth on Ti metal surfaces, the growth time and C_{60} flux dependence were studied. The growth temperature was kept at 1400 °C during these experiments. First, the C_{60} flux was held at 1.6×10^{-7} Torr while the growth time varied. As growth time increased, the 2D peak position shifted linearly to lower wavenumber. After 30 min. growth, the 2D peak was located at ~2712 ± 5 cm⁻¹. With longer growth time (90 min.), it shifted to 2705 ± 1.5 cm⁻¹. The FWHM of the 2D peak showed similar behavior to peak position. The value of the FHWM decreased from 71 ± 9 cm⁻¹ (30 min. growth) to 56.5 ± 2 cm⁻¹ (90 min. growth). The quality of the graphene was estimated from the ratio of the D and G peaks. The growth time dependence of the D/G ratio also exhibited similar behavior to position and FWHM of the 2D peak. Increased growth time resulted in a decrease of the D/G ratio from 0.32 ± 0.07 (30 min. growth) to 0.23 ± 0.01 (90 min. growth). The C_{60} flux dependence with two different fluxes was also evaluated. The growth was done at 1400 °C for 2 hr. With increasing flux from 0.8×10^{-7} to 1.6×10^{-7} Torr, we observed improvement of graphene quality with a decrease of the D/G ratio and 2D FWHM by 40% and 20%, respectively. The peak position also shifts to lower wavenumber from 2706 cm⁻¹ to 2703 cm⁻¹. Next, the effect of O_2 intercalation at 500 °C at various times was studied with Raman analysis. The 2D peak position shifted slightly to lower wavenumber. A 4 hr. intercalation led a 2D peak shift of only 5 cm⁻¹, to lower wavenumber. The 2D FWHM showed entirely different behavior. Initially it broadened compared to that of as-grown graphene (12 ± 5 cm⁻¹ for 45 min. intercalation) and then started to narrow (13 ± 3 cm⁻¹ for 2 hr. intercalation). The graphene quality variation was estimated by comparing the D/G ratio before and after intercalation. We did not observed any variation of the ratio for intercalation up to 60 min. but a significant increase was observed beyond 60 min.

The comparison of graphene grown on Ti and TiO₂ surface. Graphene growth was attempted on both Ti and TiO₂ surfaces. Figure 2 shows (a) C 1s, and (b) Ti 2p regions of the X-ray photoelectron spectroscopy (XPS) spectra after C_{60} deposition on both TiO₂ (red color curve) and Ti (blue color curve). As seen in Fig. 2a, the C 1s region exhibits two distinct peaks, located at 284.7 eV and 281.5 eV, on both
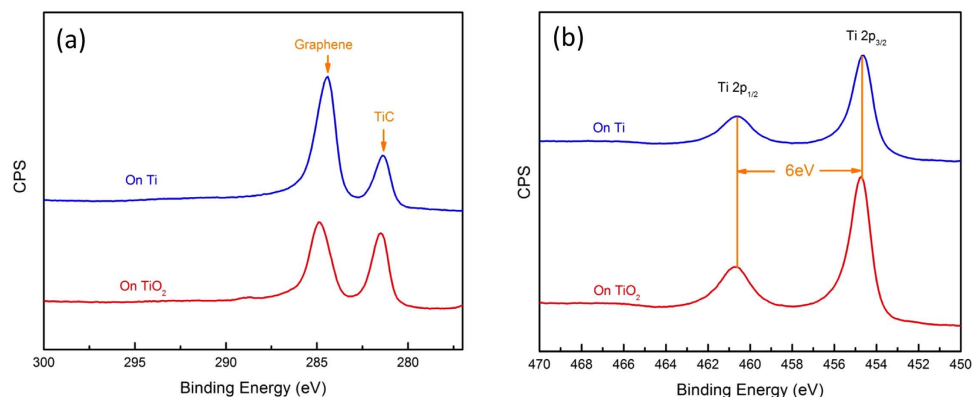
Figure 2. XPS spectra of graphene grown on Ti metal and TiO₂ surface. (**a**) High resolution C 1s spectra for Gr/Ti (blue color) and Gr/TiO₂ (red color). C 1s peaks for graphene and TiC are located at 284.7 eV and 281.5 eV on both surfaces, respectively. (**b**) Ti 2p spectra of Gr/Ti (blue color) and Gr/TiO₂ (red color). $Ti_{3/2}$ and $Ti_{1/2}$ doublet lines are located at 459.1 eV and 464.8 eV, respectively.

surfaces. The higher and lower binding energy peaks are attributed to graphene and TiC, respectively. Typical Ti $2p_{3/2}$ and Ti $2p_{1/2}$ peaks for TiO₂ are located at 459.1 eV and 464.8 eV respectively. However, our results (Fig. 2b) show the doublet peaks are located at 454.7 eV and 460.7 eV. The peak positions and 6.0 eV peak separation of the Ti 2p doublet agree well with those of TiC[12]. The O 1s peak for TiO₂ is typically located at 530.6 eV but our measurement (not shown here) shows no O 1s peak corresponding to TiO₂. Therefore, we conclude that C₆₀ deposition results in graphene and TiC formation on both Ti and TiO₂. The formation of TiC upon C₆₀ deposition could be explained by a carbon thermal reduction reaction[13]. A Gibbs free energy calculation[13] shows that TiO₂ reacts with carbon to form TiC and releases CO gas above 1300 °C. The high substrate temperature (1400 °C) during C₆₀ deposition could initiate carbon thermal reduction reactions between molecular C₆₀ and the TiO₂ surface.

Intercalation Experiments. Intercalation between epitaxial graphene and its substrate has been widely studied as a method of decoupling the strong interaction from the substrate[14–17], to modify the chemical composition of the layer under the graphene[18], and to enable exfoliation[19]. Furthermore, TiO₂ has been obtained from oxidation of TiC in the temperature range from 623 K to 1073 K in air[20]. Consequently, the conversion of TiC into TiO₂ was accomplished with an O₂ intercalation procedure. Intercalation was conducted under controlled O₂ pressure (10^{-4} Torr) in the XPS chamber (details in Method). Figure 3 shows the evolution of the (a) C 1s, (b) Ti 2p, and (c) O 1s spectra as O₂ intercalation progressed. Besides peaks for as-grown graphene at 284.7 eV and TiC at 281.5 eV, three peaks associated with C-O (286.1 eV), C=O (288.1 eV), and the $\pi \rightarrow \pi^{*}$ (291.5 eV) transition were observed in the C 1s spectra (not shown here). Since oxygen-carbon bonding was observed in the as-grown sample as well, the existence of C and O bonding might be due to air exposure during transfer from the growth chamber to the XPS chamber. In as-grown graphene/Ti structure, graphene peak is located at 284.7 eV with ~1.2 eV FWHM. However, the shift of peak position to 284.2 eV and the FHWM narrowing from 1.2 eV to 1 eV were observed as intercalation proceeds. We attribute the shift in binding energy to substrate interactions between the Ti and TiO₂. The conversion of TiC into TiO₂ during intercalation is shown in Fig. 3b. The Ti^{4+} cation doublet located at 458.8 eV and 464.6 eV and the metallic type bonding (titanium carbide) Ti^{0} peaks located at 454.7 eV and 460.9 eV were observed. These peaks are associated with Ti $2p_{3/2}$ and Ti $2p_{1/2}$ transitions, respectively. The evolution of chemical composition at different temperatures and intercalation times is also shown in Fig. 3a–c At 500 °C, the TiC C 1s peak intensity decreases as intercalation proceeds as seen in Fig. 3a (three curves on the bottom). This peak was still observable after 12 hrs. of intercalation at this temperature. A higher intercalation temperature yielded a more rapid reduction of the TiC peak intensity. At 700 °C, the TiC peak disappeared after a 2 hr. intercalation while 6 hr. intercalation was required at 600 °C. During the initial stage of intercalation, we observed two oxide states such as Ti^{4+} and Ti^{3+} along with TiC peaks (Detail in Supplementary Information). TiC related peaks in the C 1s and the Ti 2p spectra were not observed after 6 hr intercalation at 600 °C, which indicates a full conversion of TiC into TiO₂. A further increase of temperature to 700 °C showed even faster conversion of TiC than was observed at 600 °C. The 2 hr. intercalation fully converted all of the metallic TiC layers into insulating TiO₂ layers as shown in Fig. 3 (top two curves in each panel). The O 1s peak (Fig. 3c) for TiO₂ starts to appear after 1 hr intercalation (not shown here) and its peak intensity increases with further intercalation. We calculated the activation energy for TiO₂ conversion by O₂ intercalation and graphene etching by the O₂ (detail in Method). The calculated activation energy for TiO₂ conversion is about 0.29 eV while activation for graphene etching is 0.41 eV, which indicate that TiO₂ conversion is the dominant reaction in our intercalation experiments.
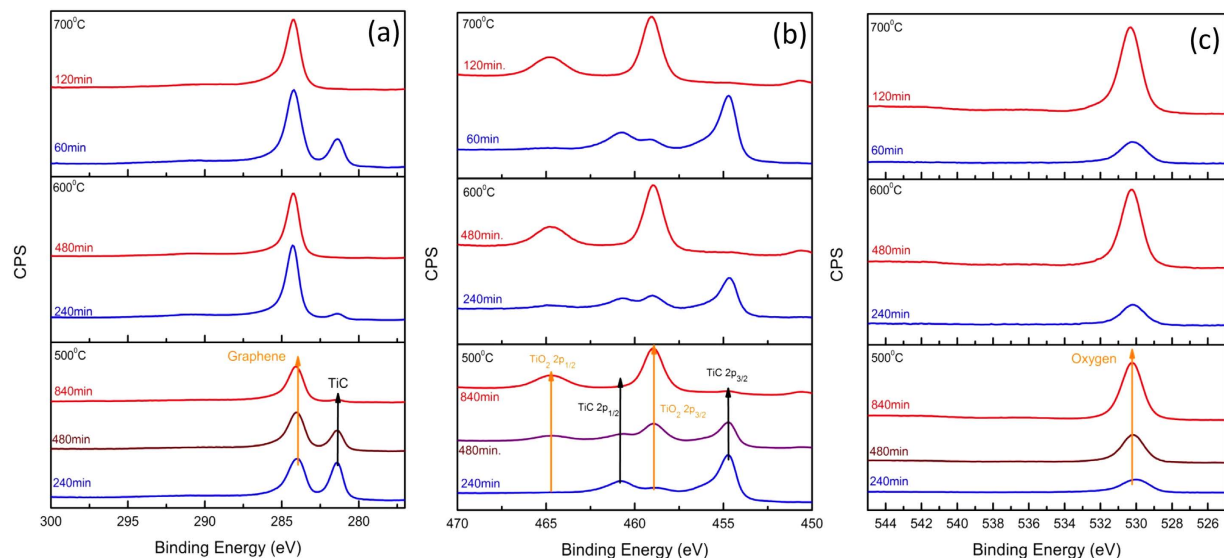
Figure 3. The temporal evolution of C 1s, Ti 2p, and O 1s XPS spectra during O_2 intercalation at three different intercalation temperatures ($500\,^0C$, $600\,^0C$, and $700\,^0C$). Three samples (Gr/Ti/n-SiC) grown at the same growth condition were used for each temperature dependent experiment. At each intercalation temperature, the spectra were normalized to TiC C1s peak, TiC Ti $2p_{2/3}$, O1s peak of bottom spectrum (blue colored curve) in the each panel. (**a**) The change of carbon C1s a as function of temperature and time. (**b**) The transition from TiC to TiO_2 during O_2 intercalation. Ti 2p doublet of TiC diminishes and that for TiO_2 start to appear as O_2 intercalation proceeds. (**c**) The enhancement of O 1s peak intensity associated with TiO_2 as O_2 intercalation proceeds.
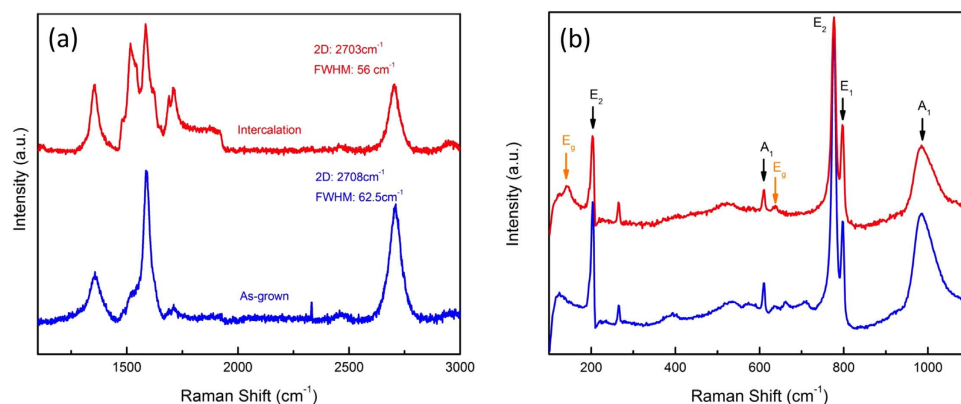

Figure 4. Raman characteristics of C_{60} deposition on Ti metal surface. O_2 intercalation was performed under 1×10^{-4}Torr oxygen partial pressure. (**a**) Comparison of Raman spectra between as-grown and O_2 intercalated samples. Intercalated sample showed 2D peak shift to lower wavenumber and narrowing of 2D peak. (**b**) The Raman signature of TiO_2 formation after O_2 intercalation. The anatase TiO_2 Raman signature (E_g vibration mode) was clearly observed.

Raman Analysis. The C_{60} deposition on Ti metal and O_2 intercalation were also investigated with Raman measurements. Figure 4 exhibits Raman spectra for an as-grown heterostructure and one intercalated under O_2 exposure. In the as-grown sample, Raman measurements show the typical Raman fingerprint of graphene with the presence of the 2D, G, and D peaks. Importantly, a fit to the 2D peak gave a single Lorentizan at $\sim2700\,cm^{-1}$. Typically, C_{60} deposition on SiC resulted in Bernal stacked few layer graphene[21] and a 2D peak best represented by multiple Lorentizans centered at $\sim2750\,cm^{-1}$. This suggests that graphene on Ti metal is not Bernal stacked but is very similar to turbostractic stacking of graphene[20]. After O_2 intercalation (Fig. 4a, red color spectrum), the 2D peak shifted to lower wavenumber and the FWHM decreased. The formation of underneath TiO_2 layer ($E_g = 3.2\,eV$) after O_2 intercalation enhances the transmittance of visible incident Raman laser into SiC substrate. It results in Raman activation of SiC
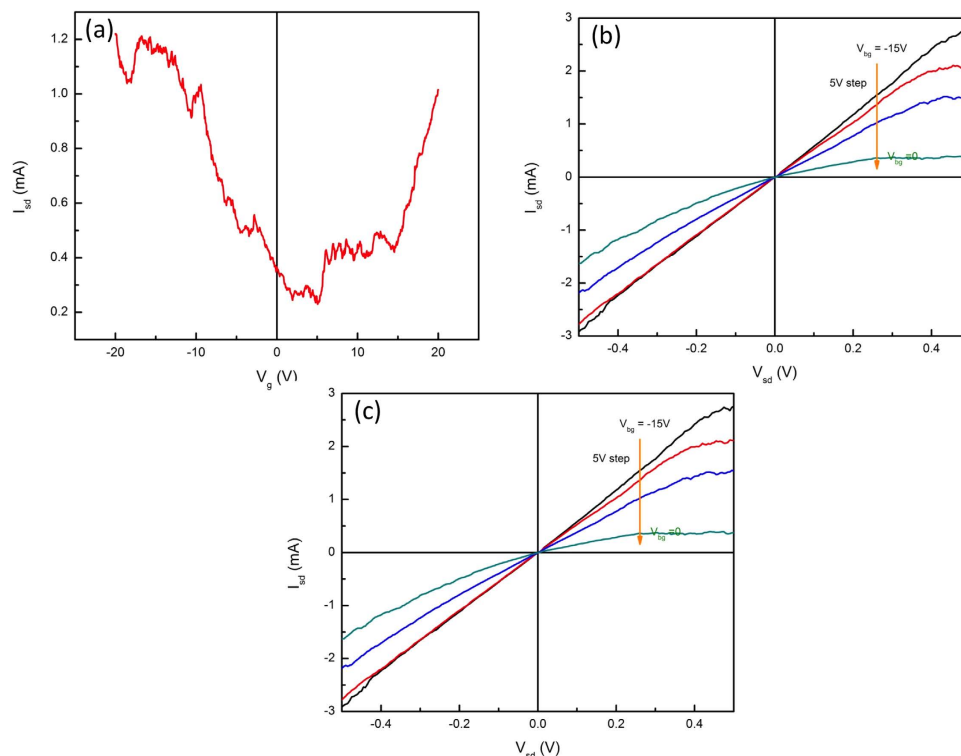
Figure 5. Room temperature electrical characteristics of bottom gated Gr/TiO₂ FET device with a large area graphene channel. (**a**) Transfer characteristics (I_{sd} vs V_g) of Gr/TiO₂ FET at $V_{sd} = 0.2$ V. The charge neutral point was observed at ~4 V. (**b,c**). I_{sd} vs. V_{sd} output characteristics at negative and positive back gate voltage (V_{bg}), respectively. V_{bg} was swept from -15 V to 0 V and from 5 V to 15 V with 5 V step, respectively.

substrate and convolution of SiC and graphene Raman spectrum. The formation of TiO₂ after intercalation was confirmed by observation of TiO₂ vibration modes (Fig. 4b). TiO₂ has several Raman active vibration modes at 143 cm⁻¹ and 640 cm⁻¹ (E_g), an A_{1g} and B_{1g} mode doublet at 516 cm⁻¹, and a B_{1g} mode at 399 cm⁻¹ [22]. Other than the graphene peaks, as-grown graphene only showed SiC Raman peaks such as the E_2, A_1, and E_1 modes (black colored annotations), while two distinct TiO₂ related Raman peaks (orange color annotations) were observed after O₂ intercalation. The peaks at ~143 cm⁻¹ and ~640 cm⁻¹ are attributed to the E_g mode (O-Ti-O bending vibration) of anatase TiO₂.

Field Effect Transistors with Gr/TiO₂ heterostructure. To explore the electrical properties of our Gr/TiO₂/n-SiC heterostructures we fabricated bottom gated FET devices. Ti/Au contacts were deposited for source and drain contacts on top of the 1 cm × 1 cm samples. The channel length was about 6 mm. The schematic diagram of GFET structure is shown in Fig. 1b. First, the gate leakage current was measured to ensure isolation between the graphene and the n-SiC substrate. The measured gate leakage current was on the order of picoamps over the gate voltage range of ±10 V (See supplementary Information), indicating strong isolation was provided by the TiO₂. The gate response was measured for a gate voltage range of ±20 V and is shown in Fig. 5a. Starting with hole-doped graphene the current flow between the source and drain decreases as the gate voltage decreased to ~3 V. Beyond this voltage, the source-drain current starts to increase as gate voltage goes negative, showing the characteristic V-shaped ambipolar behavior of graphene. The charge neutral point (CNP) occurs at $V_g \approx +3$ V, which indicates that the intercalated graphene exhibits hole doping. Figure 5b and c show that our GFET device exhibits typical transfer characteristic of FET devices. Gate modulation experiments were performed in both hole and electron doped regimes. The drain voltage was swept from -0.5 V to 0.5 V. In the hole doped region, the gate voltage was varied from -15 V to 0 V with 5 V steps. As shown in Fig. 5b, reasonable gate modulation was demonstrated. Opposite behavior was observed in the positive gate voltage region (Fig. 5c). Here, the source-drain current increased as gate voltage increased. Note that large drain current was obtained at low drain voltage and gate voltage ($I_d \approx 2.9$ mA at $V_g = 15$ V and $V_d = 0.5$ V). These results might be due a high capacitance due to the TiO₂ dielectric layer.

Photosensitivity of Gr/TiO₂ Heterostructure. In addition to its electronic device applications as a gate dielectric material, TiO₂ has been widely used as photosensitive material. However, its large bandgap (3.2 eV) has restricted its use to ultraviolet applications since the photo response is only activated under ultraviolet radiation. Several approaches have been proposed to extend its photo response to a
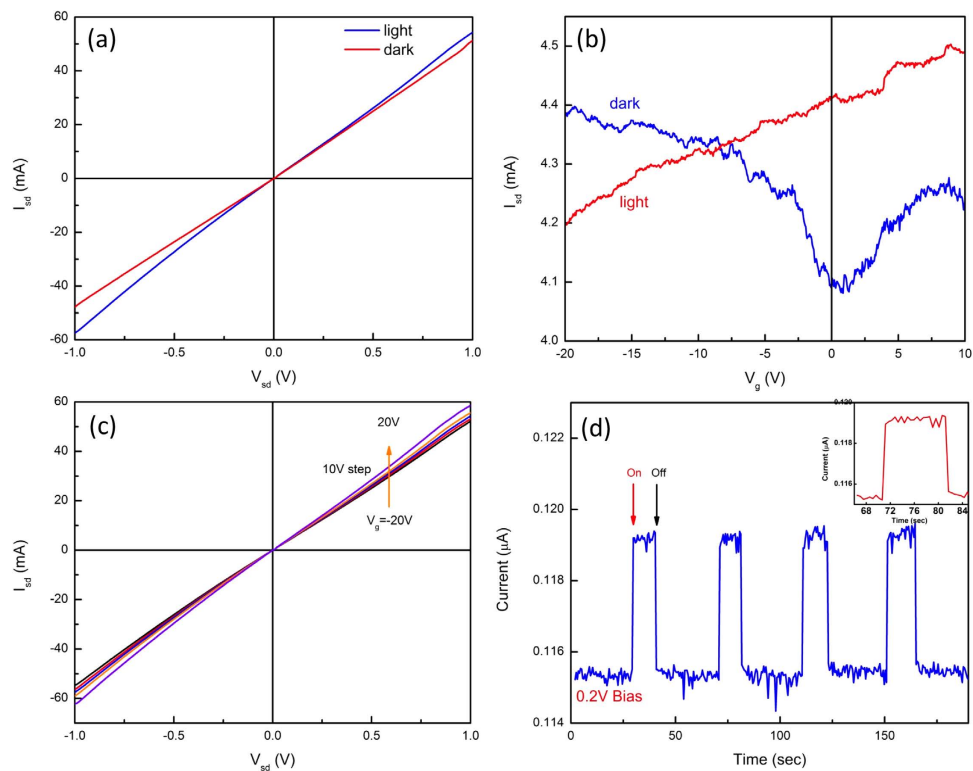
Figure 6. Photo-response of Gr/TiO$_2$ heterostructure at zero gate voltage. (**a**) I$_{sd}$ vs. V$_{sd}$ output characteristics in the dark (red color plot) and under visible light illumination (blue color plot). (A) white LED (P$_o$ = 36 mW) was used to illuminate the device. (**b**) The comparison of transfer characteristics (I$_{sd}$ vs V$_g$) in the dark (red color plot) and under illumination (blue color plot) at V$_{sd}$ = 0.2 V. In the dark, the Gr/TiO$_2$ heterostructure showed typical graphene ambipolar transfer characteristics. Under illumination, a linear transfer characteristic is exhibited, (**c**) Output characteristic of Gr/TiO$_2$ heterostructure under illumination at different gate bias voltages from -20 V to 20 V with 5 V steps. (**d**) The on/off temporal response of Gr/TiO$_2$ heterostructures at zero gate bias. V$_{sd}$ = 0.2 V was applied during measurement. Insert: the zoomed plot showing fast photo-response behavior.

broader range such as dye sensitization, doping, and coupling with semiconductors[23–25]. To explore possible photonic applications we measured the photosensitivity of our Gr/TiO$_2$/n-SiC heterostructures at room temperature (RT). The schematic diagram of measurement is shown in Fig. 1c. Figure 6a compares the I–V curves with and without visible light illumination under zero gate bias voltage. A white light LED (Power ~36 mW) was used for illumination and the source-drain bias voltage was swept from -1V to 1V. In the dark, a linear I–V relation was measured with 0.048 Ω^{-1} conductance. Upon illumination, the device showed an increased current flow through the source-drain contacts with increased current flow at high bias voltage. The conductance of the graphene improved to 0.06 Ω^{-1}, indicating a visible light photoresponse in our heterostructure. The calculated photo-responsivity of the heterostructure is about 278 mAW^{-1}, which is much higher than that reported for modified graphene photo-detectors such as graphene metal junctions (6.1 mAW^{-1})[26], graphene p-n junctions (10 mAW^{-1})[27] and biased graphene (0.2 mAW^{-1})[28]. Note that our measurements were performed with a low intensity white LED light while modified graphene photo-response experiments were conducted under illumination from a high intensity laser source. The gate response under gate bias with and without light illumination is shown in Fig. 6b. In the dark, the transfer characteristic exhibited typical ambipolar behavior of graphene. The CNP was ~ + 1.5 V, indicating hole doping of the graphene layer. Under illumination, however, the response changed entirely. The source-drain current increased continuously as the gate voltage was varied from -20 V to 10 V. Multiple devices tested under the same conditions showed similar behavior. At positive gate voltage, the photoconductivity becomes much higher than that of the negative gate voltage region because photon induced electrons increase the net charge flow through the graphene. In the negative gate voltage region the induced holes reduce the net current between the source and drain. The output characteristics under illumination as shown in Fig. 6c clearly show the increase in photo-induced conductivity. While the gate voltage changed from -20 V to 20 V, the drain current also increased, corresponding to the increase of photo-conductivity. At V$_g$ = -20 V, the graphene photoconductivity resulted in a conductance of 0.052 Ω^{-1} while it increased to 0.06 Ω^{-1} at 20 V. The difference between negative and positive gate voltage might be related to variations of net current flow through the channel. The response

to turning the light on and off was measured under 0.2 V bias between source-drain as shown in Fig. 6d. The gate voltage was set to zero volts. Upon turning the light on the photocurrent sharply increased. When the light was turned off, the photocurrent quickly dropped to the dark state. The rise and fall times of our device were about 0.4 s. The fast temporal response is quite different from that of bare graphene and graphene hybrid photo-detectors that have a slow response to external light illumination with typical rise and fall times of several seconds[29]. Since the photo-excited electron-hole pairs in graphene recombine very rapidly due to the symmetrical electrode structure, the low light absorption (2.3% per mono-layer) of graphene, and the zero bandgap, the photo-response of graphene is weak. To improve its response, modified graphene structures such as graphene-metal junctions, graphene p-n junctions, graphene coupled to waveguides, and biased graphene have been proposed but the reported photo-responsivity is still in the range of 10 mAW^{-1}, which is lower than that of our photo detector. Since the large bandgap (3.2 eV) of TiO_2 does not allow for a photo-response to visible light, the photo-response observed here might originate from the Gr/TiO_2 heterostructure. A possible mechanism for the enhanced visible light photoresponse seen in our Gr/TiO_2 heterostructures may be provided by Geng, Liu and Yao[30]. In an attempt to explain the reported visible light photocatalytic effect of TiO_2/graphene composites they calculated the electronic properties of atomic scale TiO_2 clusters on graphene films and predicted anchoring of the clusters by charge rearrangement at the interface due to an interaction between the Ti 3d orbitals of the TiO_2 and the p orbital of the graphene sheet. This results in extra states in the bandgap of TiO_2 which enable absorption of visible light by the composite and the transfer of photoexcited electrons from the TiO_2 valence band to the graphene conduction band. The subsequent separation of electrons and holes in graphene and TiO_2 leads to long carrier lifetimes. In addition, since the interface between TiO_2 and graphene plays a critical role, they also suggested that increasing the interface contact area could improve the photo response. We speculate that a similar process may be taking place in our comparatively large area heterostructures. The absorption of light takes place primarily in the TiO_2 closest to the interface where their density of states is modified by the presence of the graphene layer. Electrons then transfer to the graphene layer and increase the electron density. The separation of electrons and holes reduces recombination and the holes in the TiO_2 can screen the gating effect under positive bias while inducing more holes in the graphene layer under negative bias, leading to a reduced photoconductivity at negative bias. This model explains our experimental results shown in the gate response characteristics (Fig. 6b). In the modified graphene photo detector structures, the temporal light on/off photo-response showed slow rise and fall times because the photo-excitation is not related to a bandgap transition[31]. Therefore, we believe the abrupt on/off response seen in Fig. 6d is likely due to transitions between the TiO_2 O 2p valence band and the graphene C 2p conduction band minimum of the Gr/TiO_2 heterostructure.

Conclusion

We demonstrated that C_{60} deposition produced graphene layers on transional metal layers (Ti) with a metal carbide interface layer (TiC). After O_2 intercalation the byproduct TiC layer was completely converted into TiO_2, which resulted in a graphene/oxide heterostructure. We showed that this heterostructure exhibits dual functional properties, showing both electronic field effect phenomena and an enhanced visible light photosensity. The field effect phenomena and enhanced photosensitivity were demonstrated in bottom gated GFET devices.

Methods

Graphene growth. Metallic titanium layers (20 nm) were grown on an n-type SiC wafers by e-beam evaporation. C_{60} molecules were deposited on the Ti layers in a high temperature molecular beam epitaxy system. The growth temperature and carbon flux were 1400 °C and 1.6×10^{-7} Torr. The growth time was 30 min. For the study of graphene growth on TiO_2 surfaces, the as-deposited Ti/n-SiC sample was annealed in an O_2 environment at 800 °C for 1 hr. The oxidation of the metallic Ti layer was confirmed by XPS analysis. The graphene growth was performed with the same growth conditions as those for Ti/n-SiC. After graphene growth, the sample was exposed to air while being transferred to the XPS chamber for O_2 intercalation experiments.

For the field effect transistor device tests, Au/Ti metal contacts (source and drain) were deposited on the graphene surface. The photo response experiment was performed by illumination with a white LED at room temperature.

Calculation of activation energy. The temporal change in atomic concentration of TiC and TiO_2 was estimated by high resolution XPS spectra. The rate constant (k) for TiO_2 formation due to intercalation was obtained by analyzing the temporal change in the ratio of TiC to TiO_2 atomic concentrations at each intercalation temperature. By fitting an Arrhenius plot (Log (k) vs. 1/T), the activation energy (E_g) for oxidation was calculated. The graphene etching effect during O_2 intercalation was monitored by the reduction of the graphene C 1s peak (284.7 eV) intensity. The etching activation energy was also calculated by estimating rate constant (k) and fitting the Arrhenius plot (Log (k) vs. 1/T). The temporal variation of C 1s ratio between as-grown and intercalated samples was used to calculate the rate constant (k) at each intercalation temperature.

O₂ Intercalation Procedure.   After graphene growth, the sample was transferred to the load-lock of the XPS system. When the background pressure of the load lock chamber reached 3.0×10^{-8} Torr the sample was transferred to the analysis chamber. After initial XPS scans were acquired the sample was transferred back into the load-lock chamber for O_2 intercalation. For the intercalation experiments research grade O_2 was introduced into the chamber with a leak valve. The background pressure in the chamber was maintained at 1.0×10^{-4} Torr. Once the desired pressure was reached the sample was heated from the backside of the sample holder with a 10.6 μm CO_2 IR laser. The laser output power was adjusted until the target temperature was reached. The temperature of the sample was measured with a pyrometer. After the intercalation the chamber was pumped down until a background pressure 3.0×10^{-8} Torr was reached. The sample was then transferred back into the analysis chamber for XPS data acquisiton.

The XPS data was acquired with an Scienta Omicron standard Mg Kα (1253.6 eV) X-ray source and Argus hemispherical analyzer. High resolution scans of the C 1s, O 1s, and Ti 2p regions were acquired at 20 eV pass energy with 0.1 eV steps. The binding energy scale was calibrated against the Au 4f$_{7/2}$ (84.0 eV) peak with an overall resolution of ~1 eV. Each spectrum was fit with a Shirley background followed by fitting convoluted Gaussian and Lorentzian peak shapes for each chemical state in the region of interest. For the C 1s graphene and Ti 2p metal peaks an additional asymetry parameter was added to the Gaussian-Lorentzian convolution. The fitting procedure consisted of a Levenberg-Marquardt routine that minimizes χ^2.

References

1. Avouris, P. Graphene: Electronic and photonic properties and devices. *Nano Lett.* **10,** 4285–4294 (2010).
2. Bonaccorso, F., Sun, Z., Hasan, T. & Ferrari, A. C. Graphene photonics and optoelectronics. *Nature Photon.* **4,** 611–622 (2010).
3. Schwierz, F. Graphene transistors. *Nature Nanotechnol.* **5,** 487–496 (2010).
4. Weiss, N. O. *et al.* Graphene: An emerging electronic material. *Adv. Mater.* **24,** 5782–5825 (2012).
5. Li, G. *et al.* Observation of Van Hove singularities in twisted graphene layers. *Nature Phys.* **6,** 109–113 (2010).
6. Xue, J. *et al.* Scanning tunnelling microscopy and spectroscopy of ultra-flat graphene on hexagonal boron nitride. *Nature Mater.* **10,** 282–285 (2011).
7. Yankowitz, M. *et al.* Emergence of superlattice Dirac points in graphene on hexagonal boron nitride. *Nature Phys.* **8,** 382–386 (2012).
8. Dean, C. R. *et al.* Hofstadter/'s butterfly and the fractal quantum Hall effect in moire superlattices. *Nature* **497,** 598–602 (2013).
9. Hunt, B. *et al.* Massive Dirac Fermions and Hofstadter Butterfly in a van der Waals Heterostructure. *Science* **340,** 1427–1430 (2013).
10. Guohong Li, A. *et al.* Observation of Van Hove singularities in twisted graphene layers, *Nature Physics* **6,** 109–113 (2010).
11. Kim, H.-S. *et al.* High Efficiency Solid-State Sensitized Solar Cell-Based on Submicrometer Rutile TiO₂ Nanorod and CH3NH3PbI3 Perovskite Sensitizer. *Nano Lett.* **13,** 2412–2417 (2013).
12. Back, T. *et al.* Pulsed-Laser Deposited Transition-Metal Carbides for Field-Emission Cathode Coatings. *ACS Appl. Mater. Interfaces* **5,** 9241–9246 (2013).
13. Swift, G. A. & Koc, R. Formation studies of TiC from carbon coated TiO2. *J. Mater. Sci.* **34,** 3083–3093 (1999).
14. Larciprete, R. *et al.* Oxygen Switching of the Epitaxial Graphene–Metal Interaction. *ACS Nano* **6,** 9551–9558 (2012).
15. Lizzit, S. *et al.* Transfer-Free Electrical Insulation of Epitaxial Graphene from its Metal Substrate. *Nano Lett.* **12,** 4503–4507 (2012).
16. Ostler, M. *et al.* Buffer layer free graphene on SiC(0 0 0 1) via interface oxidation in water vapor. *Carbon* **70,** 258–265 (2014).
17. Riedl, C. *et al.* Quasi-free-standing epitaxial graphene on SiC Obtained By Hydrogen Intercalation. *Phys. Rev. Lett.* **103,** 246804 (2009).
18. Sutter, P., Sadowski, J. T. & Sutter, E. A. Chemistry under cover: Tuning metal-graphene interaction by reactive intercalation. *J. Am. Chem. Soc.* **132,** 8175–8179 (2010).
19. Herbig, C. *et al.* Mechanical exfoliation of epitaxial graphene on Ir(111) enabled by Br2 intercalation. *J. Phys.: Condens. Mater.* **24,** 314208 (314206 pp.) (2012).
20. Choi, Y., Umebayashi, T., Yamamoto, S. & Tanaka, S. Fabrication of TiO2 photocatalysts by oxidative annealing of TiC. *J. Mater. Sci. Lett.* **22,** 1209–1211 (2003).
21. Park, J. *et al.* Epitaxial graphene growth by Carbon Molecular Beam Epitaxy (CMBE). *Adv. Mater.* **22,** 4140–4145 (2010).
22. Tang, H. *et al.* Electrical and optical properties of TiO2 anatase thin films. *J. Appl. Phys.* **75,** 2042–2047 (1994).
23. De Angelis, F. *et al.* Time-Dependent Density Functional Theory Investigations on the Excited States of Ru(II)-Dye-Sensitized TiO2 Nanoparticles: The Role of Sensitizer Protonation. *J. Am. Chem. Soc.* **129,** 14156–14157 (2007).
24. Lakshminarasimhan, N., Bokare, A. D. & Choi, W. Effect of Agglomerated State in Mesoporous TiO2 on the Morphology of Photodeposited Pt and Photocatalytic Activity. *J. Phys. Chem. C* **116,** 17531–17539 (2012).
25. Yang, M. *et al.* Nb doping of TiO2 nanotubes for an enhanced efficiency of dye-sensitized solar cells. *Chem. Commun.* **47,** 2032–2034 (2011).
26. Mueller, T., Xia, F. & Avouris, P. Graphene photodetectors for high-speed optical communications. *Nature Photon.* **4,** 297–301 (2010).
27. Gabor, N. M. *et al.* Hot Carrier–Assisted Intrinsic Photoresponse in Graphene. *Science* **334,** 648–652 (2011).
28. Freitag, M., Low, T., Xia, F. & Avouris, P. Photoconductivity of biased graphene. *Nature Photon.* **7,** 53–59 (2013).
29. Zhang, B. Y. *et al.* Broadband high photoresponse from pure monolayer graphene photodetector. *Nature Commun.* **4,** 1811 (2013).
30. Geng, W., Liu, H. & Yao, X. Enhanced photocatalytic properties of titania-graphene nanocomposites: a density functional theory study. *Phys. Chem. Chem. Phys.* **15,** 6025–6033 (2013).
31. Zheng, K. *et al.* Visible Photoresponse of Single-Layer Graphene Decorated with TiO2 Nanoparticles. *Small* **9,** 2076–2080 (2013).

Acknowledgements

Author Contributions

J.H. Park conceived the original idea, performed all experiments with co-authors, analyzed the data, and wrote the paper. T. Back performed intercalation experiments, XPS measurement, wrote the paper. W.C. Mitchel and J. Boeckl analyzed the data and wrote the paper. S. Elhamri, S. Kim, and R. Naik conducted electrical measurement. S.B. Fairchild performed XPS measurement. A.A. Voevodin analyzed the data.

Additional Information